Research Article

Weather Radar Image Superresolution Using a Nonlocal Residual Network

Haoxuan Yuan [iD],[1,2] **Qiangyu Zeng** [iD],[1,2] **and Jianxin He**[1,2]

[1]*College of Electronic Engineering, Chengdu University of Information Technology, Chengdu 610225, China*
[2]*CMA Key Laboratory of Atmospheric Sounding, Chengdu 610225, China*

Correspondence should be addressed to Qiangyu Zeng; zqy@cuit.edu.cn

Accurate and high-resolution weather radar images reflecting detailed structure information of radar echo are vital for analysis and forecast of extreme weather. Typically, this is performed by using interpolation schemes, which only use several neighboring data values for computational approximation to get the estimated value regardless of the large-scale context feature of weather radar images. Inspired by the striking performance of the convolutional neural network (CNN) applied in feature extraction and nonlocal self-similarity of weather radar images, we proposed a nonlocal residual network (NLRN) on the basis of CNN. The proposed network mainly consists of several nonlocal residual blocks (NLRB), which combine short skip connection (SSC) and nonlocal operation to train the deep network and capture large-scale context information. In addition, long skip connection (LSC) added in the network avoids learning low-frequency information, making the network focus on high-level features. Extensive experiments of ×2 and ×4 super-resolution reconstruction demonstrate that NLRN achieves superior performance in terms of both quantitative evaluation metrics and visual quality, especially for the reconstruction of the edge and detailed information of the weather radar echo.

1. Introduction

Doppler weather radar with high temporal and spatial resolution e.g., China Next Generation Weather Radar (CINRAD) provides measurements with high temporal (approx. 6 minutes) and spatial (approx. 1×1 km) resolution and have been widely applied in operational research and forecasts on medium-scale and intense precipitation weather phenomena.

However, single weather radar is susceptible to beam blocking, ground clutter, and reduced resolution at long distances due to beam broadening and averaging. As shown in Figure 1, the beam width increases with the detection distance which leads to a loss of information on sudden changes in radar echoes such as velocity changes in tornadoes and mesocyclones, as well as information on extreme precipitation intensity and gradients when detection target occurs at a distance from the observing radar [1, 2]. It is, therefore, worthwhile to improve the resolution of weather

radar data by upgrading the observation equipment and by postprocessing the observation data such as interpolation or superresolution reconstruction. Due to the long cycle and high cost of the first scheme, many scholars have conducted a lot of research on the second scheme.

In terms of interpolation methods, Ruzanski and Chandrasekar [3] proposed a kernel-based Fourier interpolation method, which effectively improves the spatial and temporal resolution of weather radar by adding windows to screen the effective input data to be interpolated. Sharifi et al. [4] proposed a downscaling method based on spline interpolation to address the problem of too coarse spatial-temporal resolution when satellite precipitation estimates are applied to small areas, which effectively improves the resolution of precipitation data products while accurately capturing detailed precipitation patterns and information. Considering the non-Gaussian and locally coherent structure of weather radar reflectivity data in the wavelet domain, Kou et al. [5] proposed an interpolation method to improve
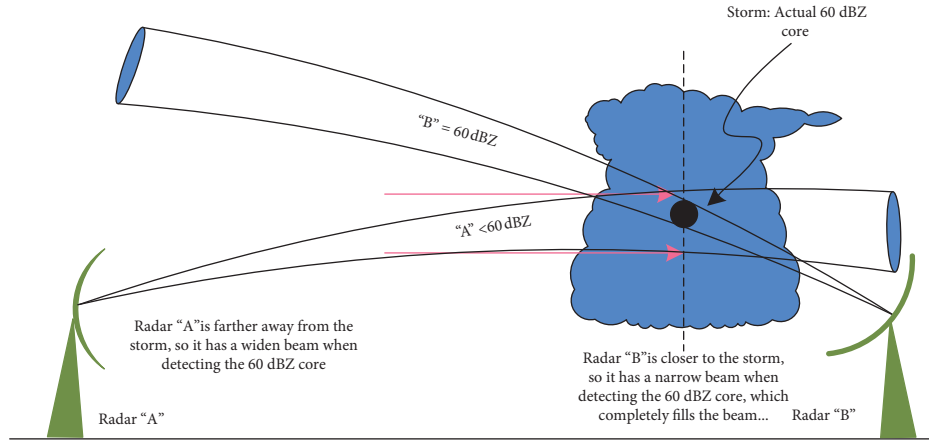
Figure 1: The effect of beam broadening.

the resolution of radar reflectivity data, which effectively use the hidden Markov tree (HMT) model as priority information to well capture the multiscale statistical characteristics of radar reflectivity data in small-scale intense precipitation condition.

Inspired by the sparsity of weather radar precipitation images in the wavelet domain, dictionary-based sparse regularization methods have been applied to statistical down scaling, converting coarse observation data into more refined [6, 7]. Based on sparse regularization, Zhang et al. [8] further proposed a nonlocal self-similar sparse representation (NSSR) model, which effectively uses the nonlocal self-similarity of weather radar echo during the reconstruction process. Similarly, in the research article, Yuan et al. [9] proposed adaptive regularized sparse representation for weather radar echo super-resolution reconstruction. Based on dictionary learning, Xu et al. [10] proposed a downscale method to obtain more refined short-duration precipitation data.

With the rapid progress of deep learning, the atmospheric research community has already taken advantage of the convolutional neural network (CNN)'s ability [11], such as the application of super resolution is related to the statistical downscaling of climate data. Vandal et al. [12] first applied CNN to climate data downscalling and improved the accuracy of precipitation data from 1° (100 km) to 1/8° (12.5 km) by stacking CNN-based super-resolution models. Cheng et al. [13] innovatively integrated the residual dense block (RDB) [14] with the Laplacian pyramid super-resolution network (LapSRN) [15] to exploit hierarchical features from all convolutional layers and generate a more refined climate image than Vandal's method. Geiss and Hardin [16] combined the classic "up-net" [17] with the "dense network" [18] and proposed a new deep convolutional neural network to learn large-scale precipitation features in weather radar images. The reconstructed weather radar image is superior to the traditional interpolation method in terms of both objective evaluation metrics and visual quality. Stengel et al. [19] also

used adversarial learning to significantly enhance the resolution of wind and solar data, which shows the notable performance of the generative adversarial network (GAN) in downscaling climate data.

However, there is an issue existing in most CNN-based super-resolution models. These networks use local convolutional operations to extract features, which result in a relatively small receptive field size of the network and the inability to capture the large-scale context information of weather radar image, such as the recurrence features of small-scale organized precipitation within and across different storm environments.

To address this issue, we proposed a nonlocal residual network (NLRN) on the basis of CNN, which increases the depth of the network and the efficiency in exploiting the large-scale context information of the weather radar image by applying residual learning and nonlocal operation.

The main contributions of this work are as follows:

(i) According to the nonlocal self-similarity of weather radar images, this research endowed the network's ability that allows them to fuse nonlocal information by stacking the nonlocal residual block (NLRB). In order to achieve a nonlocal operation, it embeds the nonlocal block (NLB).

(ii) The outstanding performance of residual learning has inspired us to introduce the long and short skip connections in the overall structure of the network and NLRB, respectively. It trains a deeper network, which effectively facilitates the flow of information and solves the gradient vanishing problems.

(iii) This study conducted loads of experiments on reflectivity data under different weather conditions. They justified that weather radar images reconstructed by NLRN achieved better quantitative results and visual quality by the proposed method than other SR methods mentioned in the experimental section.

The remaining part of the article proceeds as follows: Section 2 gives a brief introduction to the background that is related to the article. The framework and details of the proposed NLRN are described in Section 3. Section 4 presents the implementation details of NLRN. Several experimental results and discussions are presented to validate the effectiveness of the proposed NLRN in Section 5. Section 6 concludes the article.

2. Background

First, this section gives a concise overview of the SR methods that are related to the article. Second, we discuss the characteristic of a weather radar image. Finally, to facilitate the understanding of subsequent experimental parts by readers without a background in meteorology, we give a brief introduction to the hook echo.

2.1. Image Super-Resolution Methods. According to the means of implementation, the image super-resolution methods can be divided into three types: interpolation-based, reconstruction-based, and learning-based image super-resolution methods.

2.1.1. Methods Based on Interpolation. The basic idea of classical interpolation methods such as nearest interpolation, bilinear interpolation, and bicubic interpolation [20] is to approximate the lost image information by using the basis function or interpolation kernel, which only exploits the neighboring information. These methods often result in blurred edges and loss of high-frequency detail while reducing computational complexity.

2.1.2. Methods Based on Reconstruction. Reconstruction-base methods apply prior knowledge of image as constraint terms to the process of super-resolution reconstruction, which effectively solves the ill-posed problem of super-resolution reconstruction. Classical reconstruction-based methods are iterative back projection (IBP) [21], maximum a posterior estimation (MAP) [22], etc.

2.1.3. Methods Based on Shallow Learning. Before the deep learning is applied to image super resolution, the most learning-based methods are proposed on the basis of sparse representation such as nonlocally centralized sparse representation (NCSR) [23] and structure-modulated sparse representation (SMSR) [24], which mainly includes dictionary learning and sparse coding.

2.1.4. Methods Based on Deep Learning. In recent years, with the rapid progress of deep learning, learning methods represented by convolutional neural networks (CNNs) quickly dominate the computer vision field and have been widely applied in the fields of image recognition and segmentation [25–29]. Deep learning methods based on CNN have been popularly applied to the image super-resolution (SR) field since Dong et al. first proposed to combine CNN and super-resolution reconstruction (SRCNN) [30]. Dong et al. [31] replaced the large convolution kernel with more and smaller convolutional layers on the basis of SRCNN and introduced a deconvolution layer at the end of the network to greatly improve the training speed of the model. Benefiting from the increasing depth and complexity of networks, super-resolution networks possess increasingly better performance. The structure of the residual network (ResNet) [32] has been widely applied to effectively solve the gradient vanishing and gradient exploding problems faced by deep networks. The network proposed by Kim et al. (VDSR) [33] increases the convolutional layers to 20 layers, which apply global skip connection as well as adjustable gradient cropping strategy to solve the problem of difficult convergence of deep networks and achieve striking reconstruction results. An enhanced deep super-resolution network (EDSR) [34] further improves the results by removing the unnecessary batch normalization modules. Haris et al. proposed a deep back-projection network (DBPN) [35] exploiting iterative up-and-down sampling layers, which effectively use the interdependence of LR and HR images.

2.2. Weather Radar Image Characteristic. Statistics show that the weather radar image contains much redundant information. As shown in Figure 2, the red box in the left PPI (Plane Position Indicator) and the black box in the right PPI indicate the given patch and the patches that are nonlocally similar to it, respectively. Many similar and redundant structures can be observed between two patches (the example data are the reflectivity data of the first layer elevation angle of CINRAD-SA radar (Yancheng, Jiangsu, China, 11: 48, June 23, 2016). These data have 360 radials, and each radial has 460 range bins. This nonlocal redundant information has the effect of improving the quality of weather radar image reconstructed. As discussed above, limited by the size of the local receptive field, the convolution operation has deficiencies in the fusion of nonlocal information, resulting in the failure to effectively capture the long-range dependencies. Therefore, the network that can better fuse the nonlocal information of weather radar images has better super-resolution reconstruction performance.

2.3. Hook Echo. The Hook Echo is a well-researched radar reflectivity signature that must involve descending precipitation curtains as hydrometeors fall relative to the ambient air. As shown on the left part of Figure 3, the falling precipitation occurs on the back side of the updraft, which can be regarded as the low-level "extension of the bounded weak echo region (BWER)" [36]. It is commonly believed that the falling precipitation interacts with the mesocyclone of the storm, so it descends along an arc [37]. The right part of Figure 3 shows the radar reflectivity signatures of the hook echo. A common belief is that the hook echo is the area where tornadoes may occur in supercell thunderstorms [38, 39]. Therefore, capturing as much detailed information as possible about the hook echo can help in tornado detection and early warning forecasting.
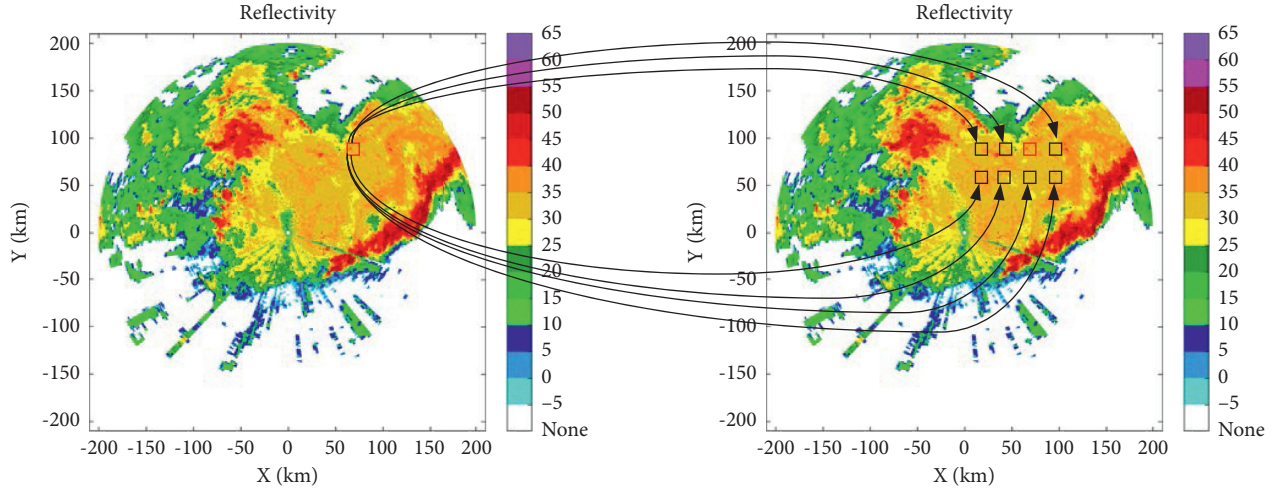
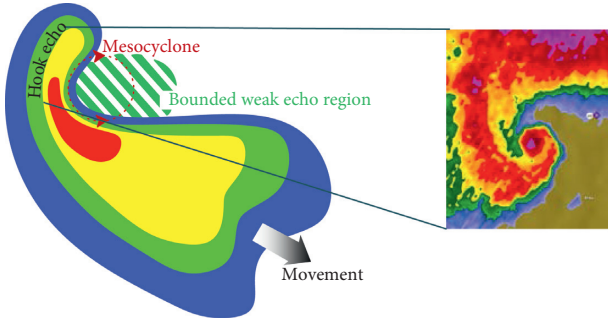FIGURE 2: Example of nonlocally similar weather radar image patches.

FIGURE 3: Conceptual model and radar reflectivity signature of hook echo.

3. Network Structure

The architecture of NLRN is illustrated in Figure 4(a), which consists of four parts: shallow feature extraction, deep feature extraction, upsampling, and reconstruction layer. I_{LR} and I_{SR} denote the input and output of NLRN. The first part extracts the shallow features F_0 from the input LR image I_{LR}.

$$F_0 = H_{SF}(I_{LR}), \qquad (1)$$

where H_{SF} denotes the two convolution operation, each followed by an activation function. To effectively solve the vanishing gradients and dying ReLU problem, we choose leaky rectified linear unit (LReLU) as the activation function. The shallow features F_0 are then used as input to the nonlinear mapping network part that consists of G nonlocal residual blocks (NLRBs) to learn mapping relations with sufficient representational ability. The structure of NLRB will be given in detail later. We formulate the deep feature-extraction process as follows:

$$F_g = H_{RNAB,g}(F_{g-1}), \quad g = 1, \dots, G, \qquad (2)$$

where $H_{RNAB,g}(\cdot)$ represents the operation of g_{th} NLRB, F_{g-1} and F_g denote the input and output of g_{th} NLRB, respectively. To make the network more focused on high-frequency information, we avoid learning low-frequency

information by adding long skip connection (LSC), which also effectively fuses shallow and deep features. The process is expressed as follows:

$$F_{G+1} = H(F_G) + F_0, \qquad (3)$$

where H represents a convolution operation and F_{G+1} as the input to the upscale module. As the previous work [34], we apply ESPCNN [40] to upscale the deep features and then use one final convolution layer with three filters to provide the final reconstructed images. The output of NLRN can be obtained by

$$I_{SR} = H_R(H_{UP}(F_{G+1})) = H_{NLAN}(I_{LR}), \qquad (4)$$

where H_{UP} and H_R denote the upsampling and the convolution operation, respectively. H_{NLAN} denotes the function of our NLRN.

3.1. Nonlocal Residual Block.
Restricted by the local receptive field size, most CNN-based SR methods have deficiencies in the fusion of nonlocal information, which result in low-efficiency utilization of self-similarity properties in images. Inspired by the classical nonlocal means [41], Wang et al. [42] proposed a nonlocal block (NLB) to fuse the nonlocal information of the image by using the self similarity of the nonlocal patches of the image, which obtain promising results in image recognition. Returning to the task of super-resolution reconstruction, in order to fully exploit the input information through the network, we propose a nonlocal residual block (NLRB). As shown in Figure 4(b), the first part of the NLRB is three convolutions with a size of 3×3, each of them is followed by LReLU. The input of NLRB and output of NLB are combined by residual learning through a short skip connection (SSC), which also effectively solves the vanishing gradient problems faced by the deep network and facilitates the flow of information.

3.2. Nonlocal Block.
Now, we present details about NLB. Nonlocal operations can transform the response of the current position into the weighted sum of all position features in the
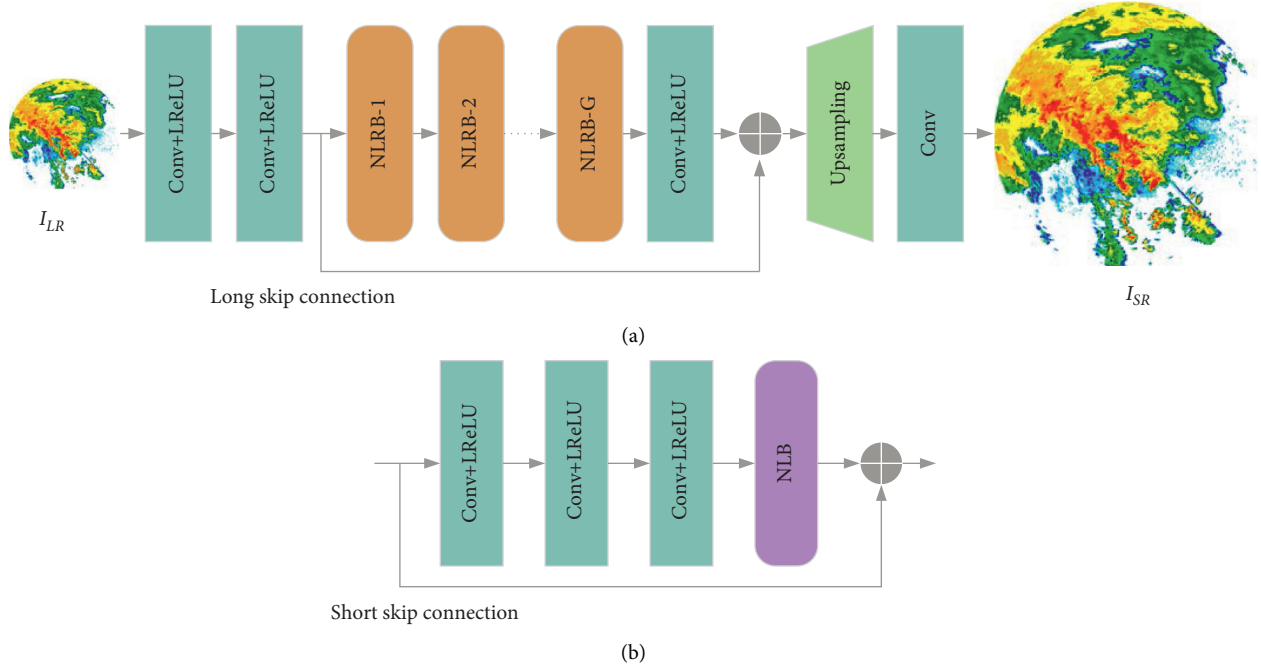
(a)

(b)

FIGURE 4: (a) The overall architecture of the proposed nonlocal residual network (NLRN). (b) The inner structure of nonlocal residual block (NLRB).

input feature map, so the nonlocal mean can fuse the nonlocal information of the image by using the self similarity of the local patch of the image. The generalization formula of the nonlocal operation in neural networks is defined as

$$y_i = \frac{\sum_{\forall j} f(x_i, x_j) g(x_j)}{\sum_{\forall j} f(x_i, x_j)}, \tag{5}$$

where i is the location index of the target output y, j is the index of all possible positions in this operation. x is the input feature mapping; y is the output feature mapping, and x and y have the same size. $f(x_i, x_j)$ represents the scalar relationship between the positions i and j. The unary function $g(x_j)$ represents the eigenvalues of the feature mapping x at the position index j. Inspired by nonlocal means and bilateral filters, we use embedded Gaussian functions to compute similarity.

$$f(x_i, x_j) = \exp\left(u(x_i)^T v(x_j)\right), \tag{6}$$

where $u(x_i) = W_u x_i$, $v(x_j) = W_v x_j$, W_u and W_v denote the weight matrices. This can be seen from the fact that for a given i, $(1/\sum_{\forall ? j} f(x_i, x_j)) f(x_i, x_j)$ becomes the SoftMax computation along the dimension j. So, we have $y_i = \text{softmax}(x_i^T W_u^T W_v x_j) g(x_j)$. For simplicity, we consider a linear embedding for $g(x_j)$: $g(x_j) = W_g x_j$, and W_g denotes the weight matrix. We further transform nonlocal operations into a nonlocal block (NLB). The definition of NLB is as follows:

$$z_i = W_z y_i + x_i, \tag{7}$$

where y_i has been given in equation (5), $+x_i$ represents a residual connection, which allows us to embed a new NLB in any pretraining model without changing its original

structure. Then, the output z at the position i of the (NLB) is calculated as follows:

$$z_i = W_z y_i + x_i = W_z \text{softmax}\left(x_i^T W_\theta^T W_\phi x_j\right) g(x_j) + x_i, \tag{8}$$

where W_z denotes the weight matrix and is initialized as zeros. The structure of NLB is illustrated in Figure 5.

3.3. Loss Function. When training NLRN, the optimal set of network parameters is obtained by minimizing the loss between training samples. To show the effectiveness of our NLRN, we choose l_1 loss function for our network optimization to provide better convergence [40]. Now, for a batch of N training images i.e. $\{I_{SR}^i, I_{LR}^i\}_{i=1}^N$, the aim is to minimize the l_1 loss function as

$$L(\theta) = \frac{1}{N} \sum_{i=1}^N \left\| I_{HR}^i - I_{SR}^i \right\|_1, \tag{9}$$

where θ denotes the parameters to be learned by the network. The Adam algorithm is applied to optimize the loss function.

4. Implementation Details

The implementation details on datasets, degradation process, training details, and evaluation metrics are presented in this section.

4.1. Datasets. We use reflectivity data from China's New Generation Weather Radar (CINRAD-SA) as a dataset. For the elevation of each layer, there are 360 radials, 460 range bins reflectivity data for each radial, and the range resolution
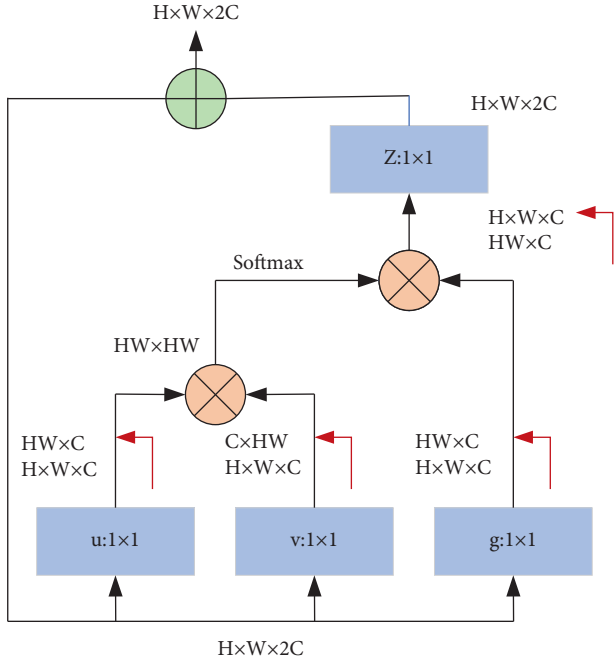
FIGURE 5: The framework of nonlocal block. Red solid line denotes matrix reshaping. $H \times W \times C$ means C features with height H and width W, and $\otimes$ denotes the matrix multiplication. $\oplus$ denotes element-wise addition.

of 1 km. To enable NLRN to learn large-scale precipitation features and small-scale extreme weather features, we use the precipitation experimental data of South China in Guangdong on May-June, 2016, the tornado and hail data of Yancheng in Jiangsu on May 27, 2008, the tornado data of Yancheng in Jiangsu on June 23, 2016 and Nantong in Jiangsu on July 06, 2016, and the typhoon data of Xuzhou in Jiangsu in August 2018. The total number of high resolution (HR) datasets with a size of 512×512 is 1800, of which 1600 images are used for training, 20 images for validation, and 180 images for testing. We mainly study the super-resolution reconstruction performance of NLRN under $\times 2$ and $\times 4$ conditions, so low resolution (LR) images with a size of 256×256 and 128×128 are obtained as input of NLRN by applying the degradation method to HR images.

4.2. Degradation Process. The weather radar image degradation process includes three processes: blurring, downsampling, and system noise. The degradation process can be formulated by the equation as follows:

$$\mathbf{y} = \mathbf{A}\mathbf{x} + \mathbf{n}, \tag{10}$$

where $\mathbf{A}$ represents the degradation operation (e.g., blurring kernel and downsampling operation), and $\mathbf{n}$ represents the weather radar receiver noise, which obeys the zero-mean Gaussian distribution.

4.3. Parameter Settings. During the training, common data enhancement methods are also used in training, such as random horizontal rotations of $90°, 180°,$ and $270°$. For every

training batch, 16 LR patches with the size of 20×20 are randomly extracted as inputs. The convolutional kernels present in the network are all 3×3 in size and 64 in number of filters. To explore the most appropriate number of G, we have counted the average PSNR under different weather conditions (e.g., the large weather system, small weather system, and cloudless) with different parameter G. As shown in Figure 6, when $G \geq 4$, the growth of PSNR becomes slow or even decreases. For balancing performance and computational complexity, we set the number of G as 4. The negative slope of leaky rectified linear units (LReLUs) is 0.1. The Adam algorithm with $\beta_1 = 0.9, \beta_2 = 0.09, \varepsilon = 10^{-8}$ is adopted to optimize the network. The initial learning rate is 10^{-4} and decreases by half for every 200 epochs. Training a NLRN on PyTorch (1.01) framework roughly takes two days with two Tesla P40 GPUs for 500 epochs.

4.4. Evaluation Metrics. In order to test the effectiveness of the proposed NLRN, we compare NLRN with several SR methods, including Bicubic, IBP, NCSR, VDSR, and EDSR. Bicubic is a classic interpolation method. IBP is a classical reconstruction method based on gradual iteration. NCSR is a traditional learning method based on sparse dictionary learning. VDSR and EDSR are CNN-based deep learning methods. Peak-signal-to-noise ratio (PSNR) (dB) and structural similarity (SSIM) [43] are used to quantitatively evaluate the SR methods.

5. Experimental Results and Analysis

In this section, we compare NLRN with other SR methods in terms of the training process, visual quality, and quantitative results.

5.1. Training Comparison. To further compare the convergence and accuracy when training VDSR, EDSR, and NLRN, the training loss curves of three networks are plotted in Figure 7(a). From Figure 7(a), it can be seen that after 100 epochs, the loss function loss decreases more slowly with iterations increasing and finally stabilizes between 6.0 and 7.0, indicating that the network has converged on the training dataset. It can be seen that NLRN has both faster convergence and better accuracy than VDSR and EDSR when training. Figure 7(b) represents the validation PSNR values of several SR methods mentioned above during the training. It can be seen that NLRN exhibited considerable advantages over the conventional methods (Bicubic, IBP, and NCSR) and CNN-based methods (EDSR and VDSR).

5.2. Visual Quality Comparison. In order to test the performance of NLRN under the large-scale weather system, we choose precipitation and typhoon reflectivity data as test data. For weather radar reflectivity data, the intense precipitation convective cells are often embedded in a lower intensity region, which shows high aggregation and sparse correlation. Figure 8 shows some of the visual results of the different SR methods under an intense precipitation
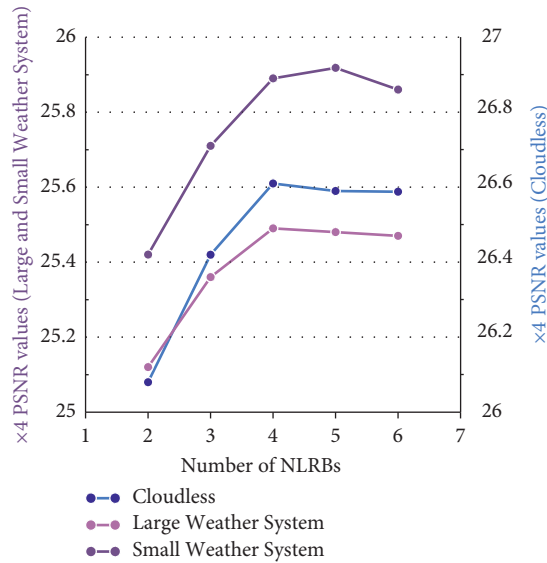
FIGURE 6: The average PSNR performance of NLRN on validation set with different parameter G (the total numbers of NLRB).
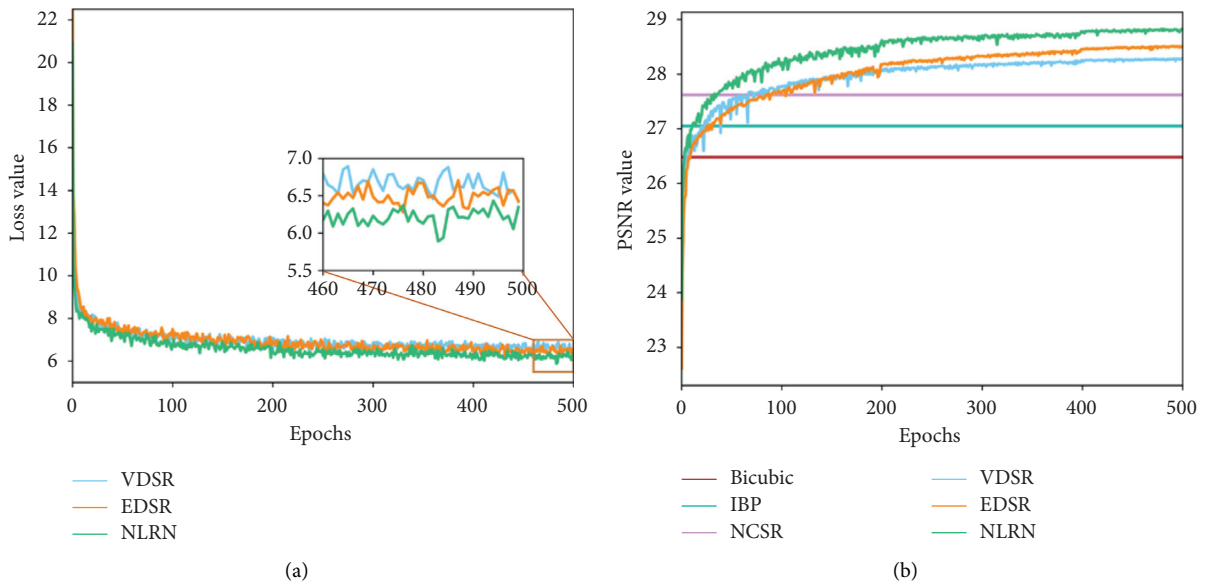

(a)

(b)

FIGURE 7: (a) Training l_1 loss of VDSR, EDSR, and NLRN for scale ×4. (b) Validation PSNR values of Bicubic, IBP, NCSR, VDSR, EDSR, and NLRN during training for scale ×2.

condition (Heyuan, Guangdong, China, 11:48, June 15, 2016). The deep learning-based output is subjectively superior to the conventional methods. The approach is not able to recover all of the very fine-scale precipitation structure that is lost when the original weather radar image is degraded. However, the deep leaning methods preserve more of the fine-scale structure and is notably better at preserving sharp edges associated with the larger features. Compared with VDSR and EDSR, NLRN effectively exploits the self similarity of radar precipitation images through the nonlocal operation, which is very useful for the identification and monitoring of intense convective precipitation echo by reconstructing high-frequency details that are prone to variability in the map, making the echo structure more refined and highlighting the location of intense echo. As

shown in Figure 9, NLRN also achieves the best subjective output under the typhoon condition

(Xuzhou, Jiangsu, China, 09:30, August 18, 2018) by reconstructing more intense echo information. To test the performance of NLRN under the small-scale weather system, we choose tornado data (Yancheng, Jiangsu, China, 14:08, June 23, 2016) as test data. From Figure 10, it can be seen that although both the conventional methods and the deep learning methods can reconstruct most of the hook echo detail information, the hook echo reconstructed by the NLRN is closer to the original hook echo, which helps forecasters to analyze small- and medium-scale extreme weather and make timely forecast and warning condition (Xuzhou, Jiangsu, China, 09:30, August 18, 2018) by reconstructing more intense echo information.
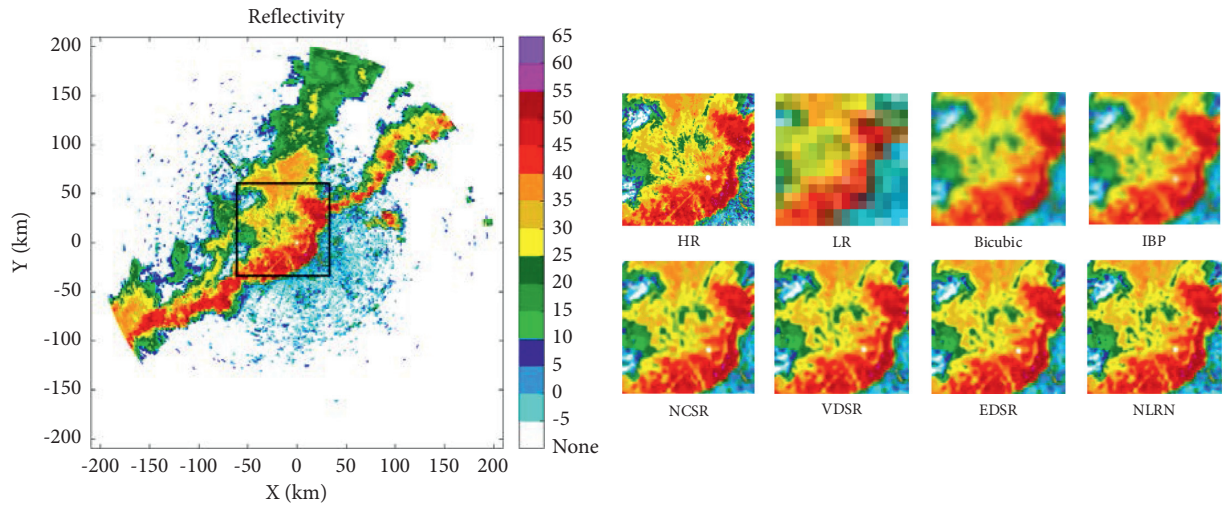
FIGURE 8: Visual comparison of ×4 super-resolution reconstruction results of intense precipitation data. The best results are in bold.
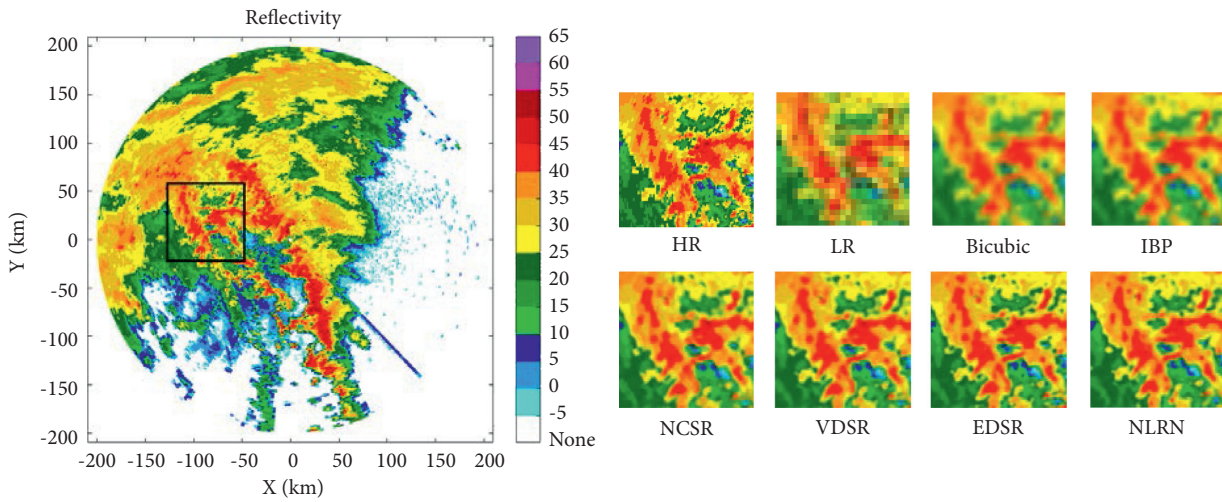

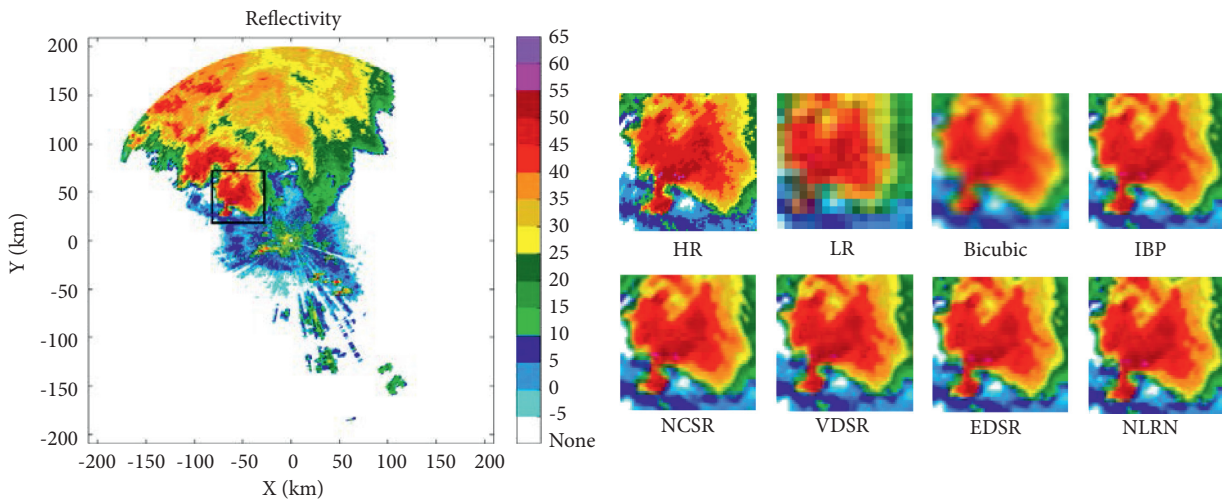FIGURE 9: Visual comparison of ×4 super-resolution reconstruction results of typhoon data. The best results are in bold.

FIGURE 10: Visual comparison of ×4 super-resolution reconstruction results of tornado data. The best results are in bold.

TABLE 1: Average PSNR (dB) of VDSR, EDSR, and NLRN for ×4 super-resolution reconstruction on test set.

Network	VDSR	EDSR	NLRN
Long skip Connection (LSC)	√	√	√
Short skip Connection (SSC)	×	√	√
Nonlocal operation	×	×	√
PSNR	25.17	25.38	**25.45**

TABLE 2: Quantitative results of the compared methods on different weather conditions.

Method	Scale	Large weather system		Small weather system		Cloudless	
		PSNR	SSIM	PSNR	SSIM	PSNR	SSIM
Bicubic	×2	26.18	0.7933	26.56	0.8012	27.89	0.8458
IBP	×2	26.67	0.7935	27.13	0.8079	28.45	0.8562
NCSR	×2	27.28	0.8233	27.65	0.8263	28.98	0.8749
VDSR	×2	28.05	0.8496	28.11	0.8492	29.31	0.8961
EDSR	×2	28.26	0.8531	28.48	0.8569	29.42	0.9013
NLRN	×2	**28.41**	**0.8546**	**28.57**	**0.8612**	**29.53**	**0.9042**
Bicubic	×4	23.21	0.6739	23.66	0.6743	25.12	0.7268
IBP	×4	23.77	0.6784	24.13	0.6803	25.43	0.7327
NCSR	×4	24.69	0.6898	24.51	0.7078	25.81	0.7513
VDSR	×4	24.83	0.7325	24.92	0.7405	26.22	0.7857
EDSR	×4	24.98	0.7382	25.08	0.7487	26.41	0.7893
NLRN	×4	**25.11**	**0.7421**	**25.19**	**0.7498**	**26.48**	**0.8013**

The best results are in bold.

5.3. Quantitative Result Comparison. Average PSNR (dB) comparison of VDSR, EDSR, and NLRN is listed in Table 1. It can be seen from the result that both EDSR and NLRN can achieve PSNR more than 0.2 dB higher than VDSR, which indicates that EDSR and NLRN with SSC have better performance in feature fusion compared with VDSR only using LSC. Furthermore, NLRN achieves better performance in exploiting large-scale context information by adding the nonlocal operation, which leads to the PSNR gain of NLRN over EDSR up to 0.07 dB. To further validate the effectiveness of NLRN, we compare the proposed NLRN with various SR methods on degraded weather radar images under different weather conditions (e.g., large- and small-scale weather system, and cloudless). All the results on ×2 and ×4 reconstruction are shown in Table 2, from which we can see that the NLRN proposed in this article can get the highest PSNR and SSIM values compared with other SR methods. Especially under the small-scale weather system, the PSNR gain of NLRN over Bicubic is up to 2 dB under ×2 reconstruction.

6. Conclusion

In this article, we proposed a nonlocal residual network (NLRN) for weather radar image super resolution, where the nonlocal residual block (NLRB) allows NLRN to integrate the nonlocal dependencies and structural information (e.g., the local and nonlocal correlations of intense precipitation echo) by inserting nonlocal blocks (NLBs) in the network. Extensive experiments on different weather conditions show the effectiveness of our NLRN in terms of quantitative and

visual results. Although NLRN cannot reconstruct exactly the same echo geometry, it can recover more accurate echo edges and details than other SR methods listed in the experimental part and highlight the structure, location, and development of intense echo, which contributes to fine detection and prediction of small- and medium-scale intense convection processes. It is worth noting that the deep learning-based super resolution of weather radar image relies not only on an excellent model structure but also on the completeness and diversity of the dataset, and that both the NLRN and the training dataset need to be further optimized to meet the increased demand for monitoring and forecasting of severe convective weather events.

Data Availability

The datasets used during the current study are available from the corresponding author on reasonable request.

Conflicts of Interest

The authors declare that there are no conflicts of interest.

Acknowledgments

References

[1] G. Ge, J. Gao, K. Brewster, and M. Xue, "Impacts of beam broadening and earth curvature on storm-scale 3D variational data assimilation of radial velocity with two Doppler radars," *Journal of Atmospheric and Oceanic Technology*, vol. 27, no. 4, pp. 617–636, 2010.

[2] Y. Averyanova, A. Averjanov, and F. Yanovsky, "Doppler polarization radar methods for meteorological applications," *IEEE Aerospace and Electronic Systems Magazine*, vol. 29, no. 7, pp. 64–73, 2014.

[3] E. Ruzanski and V. Chandrasekar, "Weather radar data interpolation using a kernel-based Lagrangian now casting technique," *IEEE Transactions on Geoscience and Remote Sensing*, vol. 53, pp. 3073–3083, 2014.

[4] E. Sharifi, B. Saghafian, and R. Steinacker, "Downscaling satellite precipitation estimates with multiple linear regression, artificial neural networks, and spline interpolation techniques," *Journal of Geophysical Research: Atmospheres*, vol. 124, no. 2, pp. 789–805, 2019.

[5] L. Kou, Y. Jiang, A. Chen, and Z. Wang, "Statistical modeling with a hidden Markov tree and high-resolution interpolation for spaceborne radar reflectivity in the wavelet domain," *Advances in Atmospheric Sciences*, vol. 37, no. 12, pp. 1359–1374, 2020.

[6] A. M. Ebtehaj, E. Foufoula-Georgiou, and G. Lerman, "Sparse regularization for precipitation downscaling," *Journal of Geophysical Research: Atmospheres*, vol. 117, 2012.

[7] E. Foufola-Giorgiou, A. M. Ebtehaj, S. Q. Zhang, and A. Y. Hou, "Downscaling satellite precipitation with emphasis on extremes: a variational ℓ1-norm regularization in the derivative domain," *Surveys in Geophysics*, vol. 35, no. 3, 2014.

[8] X. Zhang, J. He, Q. Zeng, and Z. Shi, "Weather radar echo super-resolution reconstruction based on nonlocal self-similarity sparse representation," *Atmosphere*, vol. 10, no. 5, p. 254, 2019.

[9] H. Yuan, Q. Zeng, and J. He, "Adaptive regularized sparse representation for weather radar echo super-resolution reconstruction," in *Proceedings of the 2021 International Conference on Electronic Information Engineering and Computer Science (EIECS)*, pp. 33–38, IEEE, Changchun, China, September 2021.

[10] M. Xu, Q. Liu, D. Sha et al., "PreciPatch: a dictionary-based precipitation downscaling method," *Remote Sensing*, vol. 12, no. 6, p. 1030, 2020.

[11] M. Reichstein, G. Camps-Valls, B. Stevens et al., "Deep learning and process understanding for data-driven Earth system science," *Nature*, vol. 566, no. 7743, pp. 195–204, 2019.

[12] T. Vandal, E. Kodra, S. Ganguly, A. Michaelis, R. Nemani, and A. R. Ganguly, "Generating high resolution climate change projections through single image super-resolution: an abridged version," in *Proceedings of the 27th International Joint Conferences on Artificial Intelligence Organization(IJCAI-2018)*, pp. 5389–5393, Stockholm, Sweden, July 2018.

[13] J. Cheng, Q. Kuang, C. Shen, J. Liu, X. Tan, and W. Liu, "ResLap: Generating high-resolution climate prediction through image super-resolution," *IEEE Access*, vol. 8, pp. 39623–39634, 2020.

[14] Y. Zhang, Y. Tian, Y. Kong, B. Zhong, and Y. Fu, "Residual dense network for image super-resolution," in *Proceedings of the 2018 IEEE/CVF Conference on Computer Vision and Pattern Recognition*, pp. 2472–2481, Salt Lake City, UT, USA, June 2018.

[15] W. S. Lai, J. B. Huang, N. Ahuja, and M. H. Yang, "Deep laplacian pyramid networks for fast and accurate super-resolution," in *Proceedings of the 2017 IEEE Conference on Computer Vision and Pattern Recognition (CVPR)*, pp. 624–632, Honolulu, HI, USA, July 2017.

[16] A. Geiss and J. C. Hardin, "Radar super resolution using a deep convolutional neural network," *Journal of Atmospheric and Oceanic Technology*, vol. 37, no. 12, pp. 2197–2207, 2020.

[17] O. Ronneberger, P. Fischer, and T. Brox, "U-net: convolutional networks for biomedical image segmentation," in *Proceedings of the 18th International Conference on Medical Image Computing and Computer-Assisted Intervention*, pp. 234–241, Springer, Munich, Germany, October 2015.

[18] G. Huang, Z. Liu, L. Van Der Maaten, and K. Q. Weinberger, "Densely connected convolutional networks," in *Proceedings of the 2017 IEEE Conference on Computer Vision and Pattern Recognition (CVPR)*, pp. 4700–4708, Honolulu, HI, USA, July 2017.

[19] K. Stengel, A. Glaws, D. Hettinger, and R. N. King, "Adversarial super-resolution of climatological wind and solar data," *Proceedings of the National Academy of Sciences*, vol. 117, no. 29, pp. 16805–16815, 2020.

[20] X. Xin Li and M. T. Orchard, "New edge-directed interpolation," *IEEE Transactions on Image Processing*, vol. 10, no. 10, pp. 1521–1527, 2001.

[21] P. Rasti, H. Demirel, and G. Anbarjafari, "Iterative back projection based image resolution enhancement," in *Proceedings of the 2013 8th Iranian Conference on Machine Vision and Image Processing (MVIP)*, pp. 237–240, IEEE, Zanjan, Iran, September 2013.

[22] C. Ce Liu and D. Deqing Sun, "On bayesian adaptive video super resolution," *IEEE Transactions on Pattern Analysis and Machine Intelligence*, vol. 36, no. 2, pp. 346–360, 2014.

[23] W. Dong, L. Zhang, G. Shi, and X. Li, "Nonlocally centralized sparse representation for image restoration," *IEEE Transactions on Image Processing*, vol. 22, pp. 1620–1630, 2012.

[24] Y. Zhang, J. Liu, W. Yang, and Z. Guo, "Image super-resolution based on structure-modulated sparse representation," *IEEE Transactions on Image Processing*, vol. 24, no. 9, pp. 2797–2810, 2015.

[25] K. Zhang, Y. Huang, Y. Du, and L. Wang, "Facial expression recognition based on deep evolutional spatial-temporal networks," *IEEE Transactions on Image Processing*, vol. 26, no. 9, pp. 4193–4203, 2017.

[26] O. Oktay, E. Ferrante, K. Kamnitsas et al., "Anatomically constrained neural networks (ACNNs): Application to cardiac image enhancement and segmentation," *IEEE Transactions on Medical Imaging*, vol. 37, pp. 384–395, 2017.

[27] D. Nie, L. Wang, E. Adeli, C. Lao, W. Lin, and D. Shen, "3-D fully convolutional networks for multimodal isointense infant brain image segmentation," *IEEE Transactions on Cybernetics*, vol. 49, pp. 1123–1136, 2018.

[28] D. Liu, B. Cheng, Z. Wang, H. Zhang, and T. S. Huang, "Enhance visual recognition under adverse conditions via deep networks," *IEEE Transactions on Image Processing*, vol. 28, no. 9, pp. 4401–4412, 2019.

[29] R. He, J. Cao, L. Song, Z. Sun, and T. Tan, "Adversarial cross-spectral face completion for NIR-VIS face recognition," *IEEE Transactions on Pattern Analysis and Machine Intelligence*, vol. 42, pp. 1025–1037, 2019.

[30] C. Dong, C. C. Loy, K. He, and X. Tang, "Image super-resolution using deep convolutional networks," *IEEE Transactions on Pattern Analysis and Machine Intelligence*, vol. 38, pp. 295–307, 2015.

[31] C. Dong, C. C. Loy, and X. Tang, "Accelerating the super-resolution convolutional neural network," in *Proceedings of the European Conference on Computer Vision-ECCV 2016*, pp. 391–407, Springer, Amsterdam, The Netherlands, October 2016.

[32] K. He, X. Zhang, S. Ren, and J. Sun, "Deep residual learning for image recognition," in *Proceedings of the 2016 IEEE Conference on Computer Vision and Pattern Recognition (CVPR)*, pp. 770–778, Las Vegas, NV, USA, June 2016.

[33] J. Kim, J. K. Lee, and K. M. Lee, "Accurate image super-resolution using very deep convolutional networks," in *Proceedings of the 2016 IEEE Conference on Computer Vision and Pattern Recognition (CVPR)*, pp. 1646–1654, Las Vegas, NV, USA, June 2016.

[34] B. Lim, S. Son, H. Kim, S. Nah, and K. Mu Lee, "Enhanced deep residual networks for single image super-resolution," in *Proceedings of the 2017 IEEE Conference on Computer Vision and Pattern Recognition Workshops (CVPRW)*, pp. 136–144, Honolulu, HI, USA, July 2017.

[35] M. Haris, G. Shakhnarovich, and N. Ukita, "Deep back-projection networks for super-resolution," in *Proceedings of the 2018 IEEE/CVF Conference on Computer Vision and Pattern Recognition*, pp. 1664–1673, Salt Lake City, UT, USA, June 2018.

[36] E. C. Bruning, W. D. Rust, D. R. MacGorman, M. I. Biggerstaff, and T. J. Schuur, "Formation of charge structures in a supercell," *Monthly Weather Review*, vol. 138, no. 10, pp. 3740–3761, 2010.

[37] E. N. Rasmussen, J. M. Straka, M. S. Gilmore, and R. Davies-Jones, "A preliminary survey of rear-flank descending reflectivity cores in supercell storms," *Weather and Forecasting*, vol. 21, no. 6, pp. 923–938, 2006.

[38] R. M. Wakimoto, N. T. Atkins, and J. Wurman, "The Lagrange tornado during VORTEX2. Part I: photogrammetric analysis of the tornado combined with single-Doppler radar data," *Monthly Weather Review*, vol. 139, no. 7, pp. 2233–2258, 2011.

[39] J. Wurman and K. Kosiba, "Finescale radar observations of tornado and mesocyclone structures," *Weather and Forecasting*, vol. 28, no. 5, pp. 1157–1174, 2013.

[40] W. Shi, J. Caballero, F. Huszár et al., "Real-time single image and video super-resolution using an efficient sub-pixel convolutional neural network," in *Proceedings of the 2016 IEEE Conference on Computer Vision and Pattern Recognition (CVPR)*, pp. 1874–1883, Las Vegas, NV, USA, June 2016.

[41] A. Buades, B. Coll, and J. M. Morel, "A non-local algorithm for image denoising,"vol. 2, pp. 60–65, in *Proceedings of the 2005 IEEE Computer Society Conference on Computer Vision and Pattern Recognition (CVPR'05)*, vol. 2, IEEE, San Diego, CA, USA, June 2005.

[42] X. Wang, R. Girshick, A. Gupta, and K. He, "Non-local neural networks," in *Proceedings of the 2018 IEEE/CVF Conference on Computer Vision and Pattern Recognition*, pp. 7794–7803, Salt Lake City, UT, USA, June 2018.

[43] Z. Wang, A. C. Bovik, H. R. Sheikh, and E. P. Simoncelli, "Image quality assessment: from error visibility to structural similarity," *IEEE Transactions on Image Processing*, vol. 13, no. 4, pp. 600–612, 2004.